REPORTS

MARTIAN CLIMATE

An ice age recorded in the polar deposits of Mars

Isaac B. Smith,[1]*† Nathaniel E. Putzig,[1]† John W. Holt,[2] Roger J. Phillips[3,4]

Layered ice deposits at the poles of Mars record a detailed history of accumulation and erosion related to climate processes. Radar investigations measure these layers and provide evidence for climate changes such as ice advance and retreat. We present a detailed analysis of observational data showing that ~87,000 cubic kilometers of ice have accumulated at the poles since the end of the last ice age ~370,000 years ago; this volume is equivalent to a global layer of ~60 centimeters. The majority of the material accumulated at the north pole. These results provide both a means to understand the accumulation history of the polar deposits as related to orbital Milankovitch cycles and constraints for better determination of Mars' past and future climates.

Mars undergoes oscillations in obliquity, perihelion, and eccentricity that strongly affect the planet's climate (*1*). This variability determines the amount of sunlight that reaches the surface and in turn the stability of ice at all latitudes, creating pronounced climate cycles as on Earth (*2*, *3*). Because of this high degree of activity, the north polar layered deposits (NPLD; Fig. 1) exchange substantial amounts of water with the mid-latitudes over the course of an obliquity cycle (*2*–*5*), sometimes leading to periods when Mars has abundant ice coverage over a wide range of latitudes. Unlike their terrestrial counterparts, these martian ice ages occur when the poles are warmer than average and water ice is more stable at lower latitudes, creating a widespread ground-ice "mantle" (*3*, *6*) and mid-latitude glaciers (*7*, *8*) at the same time as the polar caps retreat. During interglacial periods, the NPLD are expected to experience rapid accumulation at the expense of the mid-latitude deposits (*2*, *3*). The transitions between erosion and accumulation can leave behind unconformities, or stratigraphic sequences of truncated layers draped by continuous layers. These unconformities are observed at the surface by optical instruments (*9*–*11*) and in the subsurface by the Shallow Radar (*12*) (SHARAD) sounder onboard the Mars Reconnaissance Orbiter (*13*, *14*).

According to models of ice stability, the bulk of the NPLD, which extend to 2000 m in thickness (*15*), likely accumulated during the past ~4 million years (*1*, *2*, *4*). Most of that ice was deposited during periods without erosion, leaving continuous layers across the entire deposit (*15*, *16*). However, major unconformities are also present, and observable temporal and geographic variability in net accumulation has occurred (*13*, *14*, *17*). Obtaining age estimates for individual layers of the NPLD is an active area of research with no consensus on the best technique for determination (*17*, *18*). However, detailed stratigraphic analyses of the layers within the NPLD and south polar layered deposits (SPLD) benefit our understanding of the entire depositional system. In particular, SHARAD studies near topographic features such as the spiral troughs (*11*, *19*, *20*), Chasma Boreale (*13*), Abalos Mensa (*21*), and the basal unit (*22*) have concluded that wind was a major player in accumulation patterns of ice and dust.

Using techniques developed in previous studies (*14*, *16*) (see supplementary materials), we analyzed hundreds of radargrams [two-dimensional (2D) radar sounding profiles] of the NPLD and SPLD (fig. S1). In the north, we found cap-wide evidence for simultaneous changes in layer properties suggestive of a global shift in the climate. The most easily recognized change is a widespread, recent accumulation package (WRAP) that overlies previously eroded materials, creating an unconformity (turquoise lines in Fig. 2 and fig. S3). Immediately above the unconformity, reflectors are generally continuous [except where interrupted by troughs (*14*, *19*)] and are conformable to the erosion surface.

Also recorded at this level are changes in the slope of migration paths of features such as the spiral troughs and undulations. A migration path is a bounding surface that traces the relative horizontal and vertical position of a feature through time as seen in cross-sectional views (*19*, *20*) (dashed yellow and orange lines in Fig. 2). In many instances the migration paths increase in slope, abruptly reverse direction, or are completely buried. Previous work demonstrated that varying rates of accumulation, wind transport, and sublimation from insolation alter the migration paths of the spiral troughs (*20*); that is, the steepening of a migration path indicates a relative increase in accumulation rate. We found an increase in the slopes of migration paths at many locations along the WRAP unconformity (e.g., Fig. 2E). A more complex example includes two trough migration paths, each with an accompanying set of undulations (*11*) (Fig. 2B). Below the unconformity, both sets of undulations had migrated poleward during several hundred meters of accumulation. Above the unconformity, the

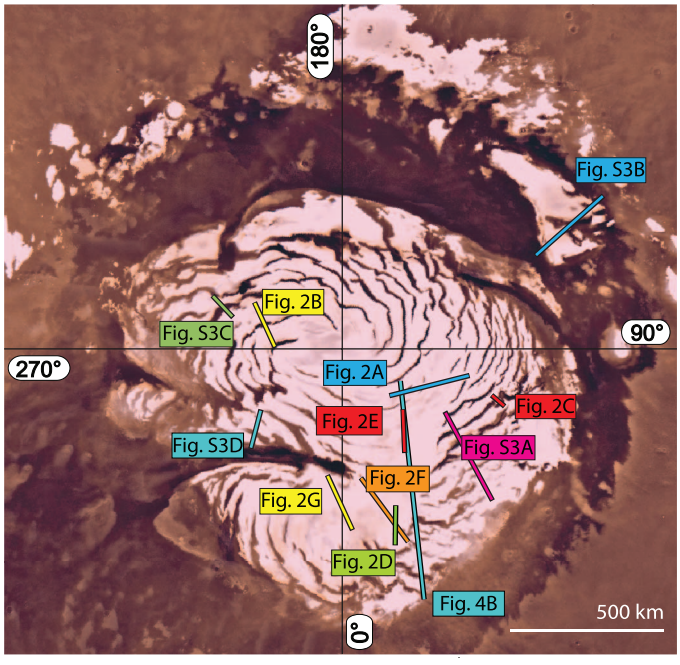

Fig. 1. Color mosaic of the north polar region from Viking Visual Imaging Subsystem data collected between 1976 and 1980 (*32*), including the north polar layered deposits (NPLD) and distal outliers. Ground-track footprints of radargrams in later figures are shown.

[1]Department of Space Studies, Southwest Research Institute, Boulder, CO 80302, USA. [2]University of Texas Institute for Geophysics, Jackson School of Geosciences, University of Texas, J. J. Pickle Research Campus, Austin, TX 78758, USA. [3]Planetary Science Division, Southwest Research Institute, Boulder, CO 80302, USA. [4]McDonnell Center for the Space Sciences and Department of Earth and Planetary Sciences, Washington University, St. Louis, MO 63130, USA.
*Corresponding author. Email: isaac@boulder.swri.edu
†Present address: Planetary Science Institute, Tucson, AZ 85719, USA.

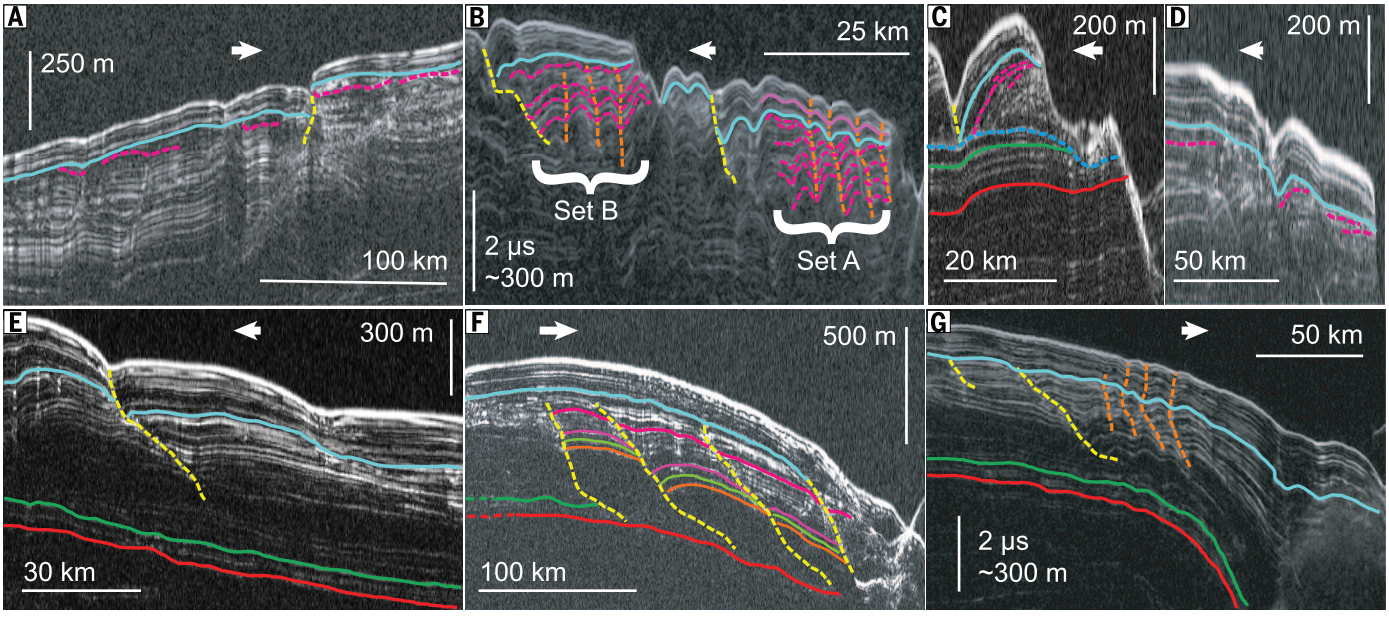

Fig. 2. SHARAD radargrams highlighting the widespread, recent accumulation package (WRAP). The WRAP unconformity (turquoise lines) is shown (**A**) within the uppermost 100 m of the NPLD, observation 1998901; (**B**) within the uppermost 90 m of the NPLD with changing properties of two sets of undulations, observation 2007101; (**C**) within the uppermost 80 m of the NPLD, observation 761602; (**D**) within the uppermost 150 m of the NPLD, observation 1247002; (**E**) with increased trough migration path slope in observation 598301; (**F**) above buried spiral troughs in Gemina Lingula, observation 725402; and (**G**) above buried spiral troughs and with reversing undulations, observation 2007101. Magenta lines, erosion and migration; yellow dashed lines, trough migration paths; orange dashed lines, undulation migration paths. Green and red reflectors are reflections 25 and 26 (R25 and R26) from (*14*), respectively. Arrows point north for each image. Ground track of each image is shown in Fig. 1. Uninterpreted radargrams are in fig. S2. Vertical exaggeration ranges between 50:1 and 150:1.

migration paths of the southernmost undulations (Fig. 2B, set A) reversed direction while maintaining approximately the same wavelength. The northern undulations (Fig. 2B, set B) were fully buried by subsequent deposition. Migration paths of undulations in Gemina Lingula also changed direction at this level (Fig. 2G), and troughs there are fully buried, leaving no detectable bounding surface with SHARAD and only minimal surface inflection (Fig. 2, F and G). Spiral troughs had previously been observed to persist continuously since their onset and often to grow in amplitude (*19*). Thus, the burial of several troughs across hundreds of kilometers represents a pronounced departure from previous climate conditions that sustained stable trough migration.

In locations where interpretations of 2D radar profiles are hindered by strong surface slopes that create interfering clutter, we analyzed data from a recently developed 3D data volume (*23*) that effectively removes such clutter to more completely map the WRAP. The 3D technique is especially powerful near 135°E at the NPLD, where clutter is abundant (*14*). With this new data set, we easily detected the WRAP as a capping unit in the uppermost hundreds of meters of the NPLD (fig. S5).

The spatial and stratigraphic distribution of the WRAP correlates with previous detections of an upper NPLD unit mapped using visible imagery of surface outcrops (*9*, *24*) in troughs (A_Bb_3 and "upper layered deposits" in those citations). Whereas those image-based mapping efforts were unable to determine the extent of and depth to the unconformity beyond the outcrops (estimating a maximum thickness of "tens of meters"), SHARAD provides the ability to trace layers through the areas between exposures at spiral troughs and accurately measure unit thicknesses.

The WRAP unconformity represents a single stratigraphic level, but subsequent regional net accumulation dictates the present depth to the unconformity. Near to the NPLD margin, where accumulation has been slower than in the interior, we find that the maximum depth to this unconformity ranges from 80 to 120 m. Closer to the center of the NPLD, where accumulation is greatest, the depth to the unconformity reaches 320 m, greater than estimates from surface observations by a factor of 10 (*9*). The average depth in areas where it exceeds 1 m is ~82 m (Fig. 3). The 1-m threshold was chosen to avoid extrapolations that extend beyond the NPLD margin as thin wedges. Additionally, we mapped basal SHARAD reflections in two thick, icy distal deposits (Fig. 3 and fig. S3B). Previous detailed geologic mapping from surface data determined that these outliers were likely deposited synchronously with the upper layers of the NPLD (*10*, *24*). Here, we measured the full extent and thickness of the deposits. Other distal deposits are widespread (topmost white regions in Fig. 3A), but they are too thin to measure with SHARAD.

We also measured recent accumulation above a shallow unconformity in the SPLD (Fig. 3B and fig. S4) and found it to be much less extensive than the WRAP in the north. The recent deposits on the SPLD are discontinuous (*25*), making it impossible to say with certainty that they accumulated simultaneously. However, the fresh appearance and lack of craters smaller than 200 m in these deposits led others to conclude that they are as young as 200,000 years (*26*). Therefore, we included them in our calculated volume of recent accumulation (Fig. 3B).

The volume of the recent north polar deposits (NPLD WRAP and outliers) is ~80,000 km^3, roughly equivalent to a global equivalent layer (GEL) of 55 cm (Fig. 3A). The SPLD recent deposits comprise 7000 km^3, contributing an additional 5 cm GEL, or 8% of the global ice flux during this period (Fig. 3B). The total contributed volume from both poles is ~87,000 km^3 or ~60 cm GEL, a sum that includes an interpolated region poleward of 87.4°N (where SHARAD cannot observe) but excludes the region poleward of 87.4°S.

Nominally, the burial of troughs and undulations by the WRAP could be attributed to a simple increase in accumulation rate, but the detection of reversing migration in some undulations tells a more complex story. Migrating undulations [niveo-aeolian antidunes (*14*, *27*)] arise in a very specific wind environment with Froude number between 0.9 and 1.2 (*20*), and a change in migration direction implies a change in Froude number. The Froude number is the ratio of the fluid speed to the speed of a gravity wave in the fluid and is determined to first order by the fluid thickness, density, and speed. From this relationship, we infer that the unconformity is the result of a shift in wind properties associated with climate change.

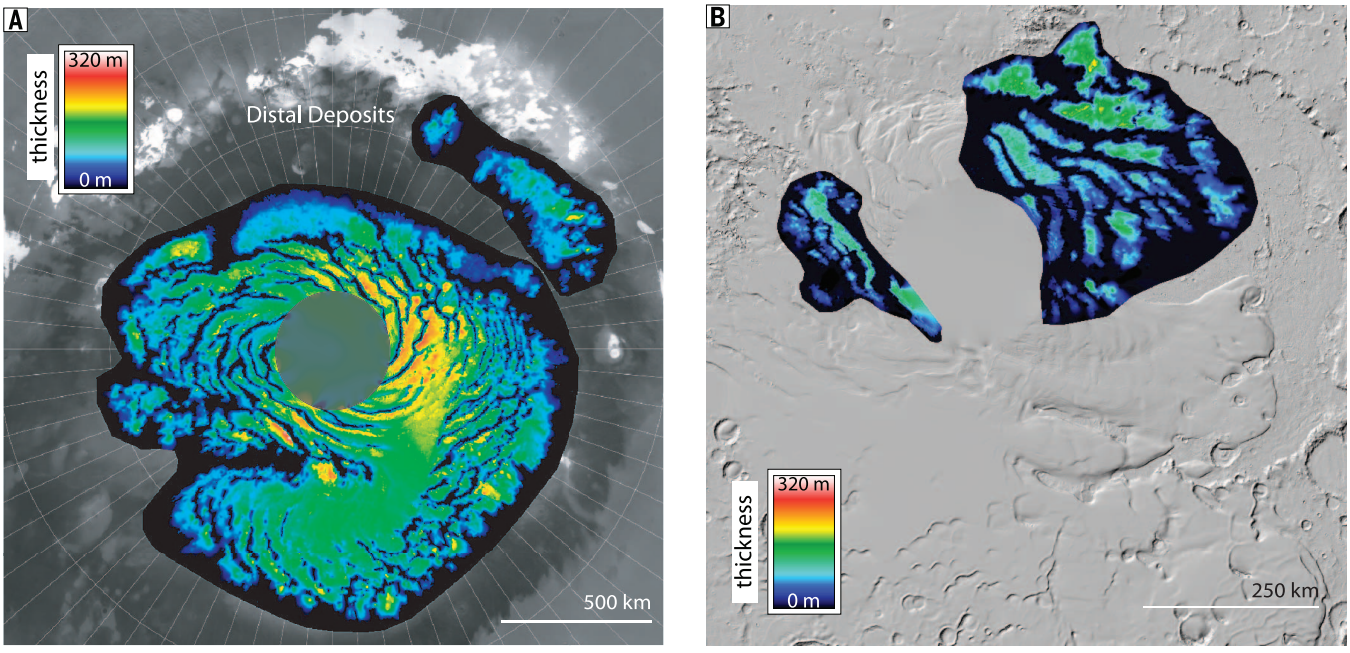

Fig. 3. Interpolated thickness maps of the NPLD WRAP, two outlier deposits, and the SPLD. (**A**) NPLD WRAP thickness ranges from 0 m at outcrops to 320 m at the NPLD interior. The integrated volume of the WRAP and outlier deposits is ~80,000 km^3. Fully interpolated region poleward of 87.4°N is shaded in gray. (**B**) Corresponding SPLD unit is discontinuous and less widespread, with a volume of ~7000 km^3. Thickness reaches 210 m locally. For maps showing uninterpolated thickness along radargram ground tracks, see fig. S1.

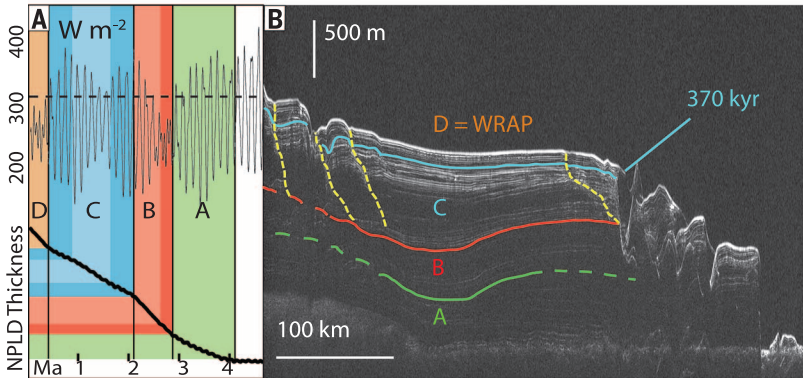

Fig. 4. Modeled ice accumulation and stratigraphic unconformities in the NPLD. (**A**) Solar insolation (W m^{-2}) correlated to ice thickness modeled for the north polar region from 4 million years ago (Ma) to the present [from (*2*)]. The accumulated thickness is shown normalized to the current NPLD value, so units are not displayed. Insolation varies by a factor of 2 through time, creating four climatologically distinct periods (vertical bars separated by colors). Applying the same logic that associates the WRAP (unit D) with the latest increase in accumulation modeled by (*2*), we assign units to periods of relatively low accumulation rates (units A and C) and relatively high accumulation rates (unit B). (**B**) SHARAD radargram 529701 annotated with stratigraphic unconformities mapped here and in (*13*, *14*). Yellow dashed line highlights spiral trough migration paths. The red reflector mapped between units B and C is reflector 29 (R29) from (*14*) and is associated with an unconformity in other locations. It represents the surface nearest which most of the spiral troughs formed. Packets of high radar reflectivity [in (B)] may correspond to darker shaded bands [in (A)] highlighting periods of greater insolation variability and potentially explaining the packet-interpacket reflectivity zones that SHARAD detects (*15*, *16*).

The discovery of a climate change recorded in the NPLD is not unexpected. Climate models predict recent and rapid north polar accumulation at the expense of mid-latitude ice loss due to obliquity changes (*2*). Those authors predicted that "the upper 300 m of the [northern] cap have accumulated during the last ~400 kyr" and that a major discontinuity "should be visible in the geological record." Although they did not provide a volume for comparison, a prior study estimated that 100 cm GEL should have been transferred from mid-latitude reservoirs to the poles over the same period (370,000 years) (*3*). The detection of mid-latitude ice reservoirs (*28*) and recent ice loss from those reservoirs (*6*, *29*) supports this hypothesis. Furthermore, detections of sublimation from fresh impacts suggest that mid-latitude ground ice is out of equilibrium with the current climate (*30*, *31*).

Our maximum accumulation finding of 320 m (and 55 cm GEL) in the north closely matches the predicted values of 300 m thickness (*2*) and 100 cm GEL (*3*). Using the modeled age of WRAP onset (370,000 years) and our maximum thickness of 320 m yields a maximum NPLD accumulation rate of ~0.86 mm/year. This value is about 3 times the published average estimates for the entire NPLD, which include periods of erosion and nonaccumulation (*17*), and it is well within the range of accelerated accumulation rates modeled for this shorter period (0.76 to 1.1 mm/year) (*2*). This implies an average transfer rate of ~0.24 km^3/year from lower latitudes to the poles, with 92% going to the north.

Our findings constitute evidence for a recent, widespread, and predominantly northern polar erosion event followed by accelerated accumulation to the present day, signaling the end of a martian glacial period. Our conclusion is supported by models that use orbital parameters to predict climate change and by observations of ongoing, mid-latitude ice loss. The total volumes transferred to the poles during this period are 55 cm GEL to the north and 5 cm GEL to the south, for a total of ~87,000 km^3 and 60 cm GEL. Besides the unconformity associated with the erosion event predating the current interglacial period, two other major unconformities and stratigraphic inflections have been mapped using SHARAD data (*13*, *14*). We infer that the processes active

today were also active in the past and suggest that these three inflection points correspond to the three predicted in models (*2*, *4*) (Fig. 4); if so, then the NPLD accumulated primarily in four climatologically distinct stages. More work is required to determine whether the lower unconformities match the predicted ages, as in the case of the WRAP, but we present them again here and revise the accumulation scenario posited by (*16*).

REFERENCES AND NOTES

1. J. Laskar, B. Levrard, J. F. Mustard, *Nature* **419**, 375–377 (2002).
2. B. Levrard, F. Forget, F. Montmessin, J. Laskar, *J. Geophys. Res.* **112**, E06012 (2007).
3. J. W. Head, J. F. Mustard, M. A. Kreslavsky, R. E. Milliken, D. R. Marchant, *Nature* **426**, 797–802 (2003).
4. R. Greve, B. Grieger, O. Stenzel, *Planet. Space Sci.* **58**, 931–940 (2010).
5. J.-B. Madeleine, F. Forget, E. Millour, T. Navarro, A. Spiga, *Geophys. Res. Lett.* **39**, L23202 (2012).
6. J. F. Mustard, C. D. Cooper, M. K. Rifkin, *Nature* **412**, 411–414 (2001).
7. J. W. Holt *et al.*, *Science* **322**, 1235–1238 (2008).
8. J. J. Plaut *et al.*, *Geophys. Res. Lett.* **36**, L02203 (2009).
9. K. L. Tanaka *et al.*, *Icarus* **196**, 318–358 (2008).
10. K. L. Tanaka, C. M. Fortezzo, Geologic map of the north polar region of Mars, U.S. Geological Survey Scientific Investigations Map 3177 (2012).
11. A. D. Howard, J. A. Cutts, K. R. Blasius, *Icarus* **50**, 161–215 (1982).
12. R. Seu *et al.*, *J. Geophys. Res.* **112**, E05S05 (2007).
13. J. W. Holt *et al.*, *Nature* **465**, 446–449 (2010).
14. I. B. Smith, J. W. Holt, *J. Geophys. Res.* **120**, 362–387 (2015).
15. R. J. Phillips *et al.*, *Science* **320**, 1182–1185 (2008).
16. N. E. Putzig *et al.*, *Icarus* **204**, 443–457 (2009).
17. K. E. Fishbaugh, C. S. Hvidberg, *J. Geophys. Res.* **111**, E06012 (2006).
18. S. Christian, J. W. Holt, S. Byrne, K. E. Fishbaugh, *Icarus* **226**, 1241–1251 (2013).
19. I. B. Smith, J. W. Holt, *Nature* **465**, 450–453 (2010).
20. I. B. Smith, J. W. Holt, A. Spiga, A. D. Howard, G. Parker, *J. Geophys. Res.* **118**, 1835–1857 (2013).
21. T. C. Brothers, J. W. Holt, A. Spiga, *Geophys. Res. Lett.* **40**, 1334–1339 (2013).
22. T. C. Brothers, J. W. Holt, A. Spiga, *J. Geophys. Res.* **120**, 1357–1375 (2015).
23. N. E. Putzig, F. J. Foss, B. A. Campbell, R. J. Phillips, *LPI Contrib.* **1791**, 1336 (2014).
24. K. L. Tanaka, *Nature* **437**, 991–994 (2005).
25. I. B. Smith, A. Spiga, J. W. Holt, *Geomorphology* **240**, 54–69 (2015).
26. M. Koutnik, S. Byrne, B. Murray, *J. Geophys. Res.* **107**, 10-1–10-10 (2002).
27. C. Herny *et al.*, *Earth Planet. Sci. Lett.* **403**, 56–66 (2014).
28. A. M. Bramson *et al.*, *Geophys. Res. Lett.* **42**, 6566–6574 (2015).
29. V.-P. Kostama, M. A. Kreslavsky, J. W. Head, *Geophys. Res. Lett.* **33**, L11201 (2006).
30. S. Byrne *et al.*, *Science* **325**, 1674–1676 (2009).
31. C. M. Dundas, S. Byrne, *Icarus* **206**, 716–728 (2010).
32. A. S. McEwen *et al.*, Global Color Views of Mars, *25th Lunar and Planetary Science Conference* (1994), pp. 871–872.

ACKNOWLEDGMENTS

Supported by the SHARAD instrument, NASA grants NNX10AQ32G (N.E.P.) and NNX11AL10G (J.W.H.), and the Institute for Geophysics, Jackson School of Geoscience, University of Texas at Austin (J.W.H.). Data used in this investigation are available at NASA's planetary data system (PDS), http://pds-geosciences.wustl.edu/mro/mro-m-sharad-5-radargram-v1/mrosh_2001/. We thank the SHARAD team and Mars polar group for supportive comments and suggestions, F. Foss and B. Campbell for their roles in generating the 3D radar volume, and Seisware International for use of its seismic mapping tools.

SUPPLEMENTARY MATERIALS

www.sciencemag.org/content/352/6289/1075/suppl/DC1
Methods
Figs. S1 to S5
References (*33*–*36*)

19 November 2015; accepted 19 April 2016
10.1126/science.aad6968

ORGANIC CHEMISTRY

Enantioselective synthesis of an ophiobolin sesterterpene via a programmed radical cascade

Zachary G. Brill, Huck K. Grover, Thomas J. Maimone*

Cyclase enzymes weave simple polyprenyl chains into the elaborate polycyclic ring systems of terpenes, a sequence that is often difficult to emulate under abiotic conditions. Here we report a disparate synthetic approach to complex terpenes whereby simple prenyl-derived chains are cyclized using radical, rather than cationic, reaction pathways. This strategy allowed us to efficiently forge the intricate 5-8-5 fused ring systems found in numerous complex natural product classes and also enabled a nine-step total synthesis of (−)-6-*epi*-ophiobolin N, a member of the large family of cytotoxic ophiobolin sesterterpenes. A small-molecule thiol catalyst was found to override the inherent diastereoselectivity observed during a reductive radical cascade cyclization process. This work lays the foundation for efficient synthesis of terpenoid ring systems of interest in medicinal research, particularly those that have been historically challenging to access.

Terpenes represent a highly diverse class of natural products whose derivatives have been developed into numerous medications approved by the U.S. Food and Drug Administration for the treatment of cancer, bacterial infection, malaria, and various other human diseases (*1*, *2*). Despite these successes, terpenes can pose distinct challenges for medicinal research because of their often-limited commercial availability, resistance to deep-seated structural modifications, and incompletely elucidated biosynthetic pathways. Owing to their nonmodular chemical structures, a unifying strategy for the chemical synthesis of terpenes does not exist, further exacerbating the difficulties of working with these compounds (*3*). Terpenes arise via the enzymatic conversion of simple polyprenyl chains into highly intricate polycyclic carbon networks of extraordinary diversity (*4*). Biomimetic synthesis, the act of emulating nature's bond construction process, would be an ideal synthetic tool in this context (*5*, *6*). Indeed, cationic polyene cyclizations are perhaps the best studied of all biomimetic cyclization reactions (*7*). To date, however, a very limited subset of terpenoid carbocyclic diversity can be accessed in this manner in a laboratory setting, and the synthesis of many medium and larger terpene ring frameworks has proven especially problematic. In contrast, shape-restricted enzyme cavities in terpene cyclases have evolved with appropriately placed amino acid residues to stabilize selective transition states and, in concert, dictate cyclization pathways. As a result of modulating this environment, the formation of myriad terpene skeletons, elaborate rearrangement processes, and various termination modes all become chemically possible (*4*). Here we describe a disparate approach, in which simple polyprenyl-derived chains are cyclized via radical-based (as opposed to cationic-based) methods. Through the use of different reagent combinations, we show that the termination modes of these cyclizations can be controlled and, with a chiral small-molecule thiol catalyst, their inherent stereochemical preferences altered.

Complex 5-8-*n* fused ring systems (*n* = 5 or 6) are found in numerous di- and sesterterpenes that possess notable antibiotic (*8*), cytotoxic (*9*), and immunosuppressant properties, among others (*10*) (Fig. 1). Central to this structural type is the continually expanding family of ophiobolin sesterterpenes featuring a stereochemically rich and synthetically formidable 5-8-5 fused ring system (Fig. 1A). Though compounds in this family were initially investigated for their phytotoxic effects, which negatively influence agricultural production, ophiobolin A (**1**) was later discovered to be a powerful inhibitor of calmodulin and remains an important tool for studying this calcium signaling protein (*11*). Most recently, these fungal metabolites have attracted much attention for their potent cytotoxic effects against multiple cancer cell lines, including the highly drug-resistant human brain tumor glioblastoma multiforme (*12*–*14*). Although more than 30 distinct members have been identified to date, often in minute and varying quantities, ophiobolin A (**1**), ophiobolin C (**2**), and 6-*epi*-ophiobolin N (**3**) highlight the major structural variations found in this terpenoid family, including (i) hydroxylation at carbon-3 or dehydration to an enone system; (ii) epimeric stereochemistry at carbon-6 for nearly all members; and (iii) myriad side-chain oxidation motifs, sometimes resulting in tetrahydrofuran (THF) ring formation (see **1**, for example) (*11*, *15*). Notwithstanding decades of research by numerous laboratories (*16*–*22*), only Rowley *et al.* (*23*) and, more recently, Tsuna *et al.* (*24*) have charted fully synthetic routes to various ophiobolin members. Despite these achievements, the long step

Department of Chemistry, University of California, Berkeley, 826 Latimer Hall, Berkeley, CA 94702, USA.
***Corresponding author. Email: maimone@berkeley.edu**

An ice age recorded in the polar deposits of Mars
Isaac B. Smith, Nathaniel E. Putzig, John W. Holt and Roger J. Phillips (May 26, 2016)
Science **352** (6289), 1075-1078. [doi: 10.1126/science.aad6968]

Editor's Summary

Evidence for ice ages on Mars

Models predict that Mars should have undergone ice ages in the past, but evidence has been scant. Smith *et al*. used radar measurements from NASA's Mars Reconnaissance Orbiter to probe the planet's polar ice caps. Clear layers within the ice allowed them to calculate how much ice was deposited at different times. The results provide evidence for a recent ice age on Mars. Understanding the martian climate will help determine when the planet was habitable in the past, and how that changed, and may inform studies of climate change on Earth.

Science, this issue p. 1075

Science (print ISSN 0036-8075; online ISSN 1095-9203) is published weekly, except the last week in December, by the American Association for the Advancement of Science, 1200 New York Avenue NW, Washington, DC 20005.